

Perturbations of Fabric Evolution and Flow of Anisotropic Ice

Hay and Waddington

Correspondence to: Michael Hay (mhay@uw.edu)

Abstract. The distribution of crystal orientations of ice grains (the crystal fabric) of a polycrystal has a strong influence on polycrystalline ice-flow, due to the plastic anisotropy of the individual grains. In turn, crystal-orientation fabric evolution is guided primarily by deformation. This suggests that the coupled dynamics of flow and fabric may produce significantly different behavior than if they were uncoupled. We develop an analytical first-order perturbation model of coupled linear flow of anisotropic ice flow and fabric evolution. We analyze the development of several types of perturbations in a range of flow scenarios. The results show that fabric development coupled to flow of anisotropic ice is dynamically unstable in many flow scenarios, with certain characteristic fabric perturbations being reinforced through feedback between deformation and fabric development. These instabilities may lead to the development of shear bands, boudinage, and other stratigraphic disturbances seen in ice sheets.

1 Introduction

An individual ice crystal has an anisotropic creep response, deforming most easily in shear parallel to the crystal basal-plane, orthogonal to the crystallographic c-axis. Plastic deformation of an ice polycrystal depends on the orientations of its constituent grains (e.g. Azuma (1994)), which is described by the c-axis orientation distribution function (ODF). The ODF is a probability distribution of c-axis density often defined on the upper hemisphere (because a c-axis vector \mathbf{c} is indistinguishable from $-\mathbf{c}$). A polycrystal with an isotropic ODF will have a bulk isotropic response to applied stress. However, polycrystals develop an anisotropic ODF in response to applied strain. Grain c-axes tend to rotate towards the axes of principal compression, due to lattice rotation. This produces a bulk anisotropic response to stress (Alley, 1992). In flank flow in ice sheets, c-axes typically cluster near vertical. This puts the basal plane in close alignment with applied shear stress, producing ice that can be several times softer under shear than isotropic ice. Vertical-maximum fabric also develops under vertical compression. Unlike with simple shear, however, the ice becomes harder to the applied vertical compression with stronger single-maximum fabrics. This is because the resolved shear stress on nearly horizontal basal planes is small under vertical compression.

Given that fabric has such a strong effect on flow, and vice-versa, it is therefore important to understand it as a coupled system rather than treating flow and fabric separately. Many complex coupled dynamical systems of physical interest exhibit instability. Examples include the gravitational n-body problem, which has unstable solutions, or Earth's weather.

There are indications that coupled flow of anisotropic ice has instabilities as well. Thorsteinsson and Waddington (2002) studied the development of low-angle stratigraphic wrinkles near ice divides. They concluded that single-maximum fabrics typical near ice divides enhance the ability of low-angle incipient wrinkles to steepen, and eventually overturn. The single-

maximum fabrics near ice divides promote horizontal shear, which steepens incipient wrinkles, and hinder vertical compression, which flattens them. Fudge et al. (2016) found evidence of boudinage in electrical conductivity measurements in the West Antarctic Ice Sheet Divide core. Boudinage thins layers, and can eventually pinch them out entirely. Additionally, boudinage could act as a source of incipient stratigraphic wrinkles in the surrounding layers.

- 5 Alley et al. (1997) found “striping” in the GISP2 core. These stripes were composed of elongated regions of grains possessing aligned, off-vertical c-axes, in a medium of vertical single-maximum fabric. In horizontal extension under divide flow, these stripes localize shear within them, and displace layers in the hard surrounding ice. Jansen et al. (2016) produced bands similar to observed stripes in strong single-maximum fabrics using microstructure modeling. These were identified as shear bands. Regions where the fabric was tilted away from the lattice-preferred orientation towards the direction of shear seeded the
10 formation of the bands. These small-scale disturbances, which have been found hundreds of meters off the bed, cannot be related to basal topography. They must arise from inhomogeneities in the ice itself.

Montgomery-Smith (2011) developed a coupled perturbation model for the orientations of slender fibers immersed in Stokes flow. It was shown that instabilities of fiber orientations can develop; this would not occur in uncoupled flow. Coupled ice flow and fabric are mathematically related to the case of fibers immersed in Stokes flow. In this paper, we derive a linear full-Stokes,
15 coupled anisotropic-flow and fabric-perturbation model to study the stability of the coupled flow and fabric system, similarly to Montgomery-Smith (2011). We show that dynamical instability of fabric coupled to ice flow can seed such disturbances.

1.1 Background

In this paper, we will make use of index notation due to the use of higher-order tensors and tensor contractions. Unless otherwise indicated, we follow the summation convention, where two repeated indices indicate a sum across that index. For example,
20 $p_i p_i$ should be read as $p_1 p_1 + p_2 p_2 + p_3 p_3$. Matrix notation is also used when it is convenient. Such quantities are denoted in bold face, whereas scalar quantities (such as in index notation expressions) are in normal face.

Preferred c-axis orientations in ice develop primarily due to intracrystalline slip. This causes c-axes to rotate away from the directions of principal extensional strain (Azuma and Goto-Azuma, 1996). ODFs are often summarized using orientation (or, moment) tensors (e.g. Svendsen and Hutter (1996)). The second-order orientation tensor A_{ij} is the expectation $\langle c_i c_j \rangle$,
25 where $i, j = 1, 2, 3$. The mean of the ODF, $\langle c_i \rangle$, is always zero because of antipodal symmetry. Therefore, A_{ij} is also the covariance matrix of the distribution, by definition of covariance as,

$$\text{Cov}(c_i, c_j) = \langle (c_i - \langle c_i \rangle)(c_j - \langle c_j \rangle) \rangle. \quad (1)$$

The diagonal elements A_{11} , A_{22} , and A_{33} give a measure of the c-axis concentration on the x , y , and z axes, respectively. Throughout this paper, the indices 1, 2, and 3 will be associated with the x -, y -, and z -directions, respectively. Similar to
30 the second-order orientation tensor, the fourth-order tensor is the expected value $\mathbb{A}_{ijkl} = \langle c_i c_j c_k c_l \rangle$. Since ODFs over the sphere are antipodally symmetric, odd-order tensors are zero. The second-order tensor can be diagonalized. The eigenvalues $\lambda_1 \leq \lambda_2 \leq \lambda_3$ sum to unity by construction. The eigenvectors, or fabric principal directions, denote the directions of greatest density (corresponding to the largest eigenvalue λ_3), smallest density (the smallest eigenvalue λ_1), and a direction orthogonal

Table 1. List of symbols

Symbol	Definition
q_i	Tensor quantity in index notation
\mathbf{q}	Same tensor in vector notation
c_i	ice-crystal c-axis for $i = 1, 2, 3$ in x, y, z directions
$\psi(\mathbf{c})$	Ice-crystal orientation dist. func.
$\langle q_i \rangle$	Expected value of q_i under ψ
A_{ij}	Second-order orientation tensor $\langle c_i c_j \rangle = \langle a_{ij} \rangle$
\mathbf{a}	Second-order orientation tensor in Voigt notation
\mathbb{A}_{ijkl}	Fourth-order orientation tensor $\langle c_i c_j c_k c_l \rangle$
λ_i	Fabric eigenvalue of A_{ij}
J_{ij}	Jacobian matrix of the perturbed fabric system
ζ_i	Eigenvalues, or growth rates, of J_{ij}
ζ_{max}	Real part of ζ_i with highest real part
V_{ij}	Vorticity tensor
D_{ij}	Strain-rate tensor
\mathbf{d}	Strain-rate tensor in Voigt notation
ϕ	Angle of rotation about the y -axis
θ	Angle of rotation about the x -axis
δ_{ij}	Kronecker delta symbol
S_2	unit sphere
\mathbb{F}_{ijkl}	viscosity tensor
σ	A standard deviation
S_{ij}	Stress tensor
ϵ	A small parameter
κ_i	Three-dimensional wavevector
\bar{y}	An unperturbed quantity
\hat{y}	The Fourier coefficient of a perturbation to \bar{y}
$\hat{\mathbf{a}}$	The Fourier coefficient of the perturbation to \mathbf{a}
$\bar{\mathbf{G}}$	Spatially homogeneous, unperturbed vel. gradient
η	Viscosity of shear along basal plane

to the other two (corresponding to λ_2). An isotropic fabric has three equal eigenvalues. A girdle fabric (in which there is a band of high concentration along a great circle) has two nearly equal eigenvalues, and one small eigenvalue. A single-maximum fabric has one large eigenvalue, and two small ones.

If the evolution of the ODF is given by a partial differential equation (PDE) over the sphere, one can integrate A_{ij} to derive an ordinary differential equation (ODE) for the evolution of A_{ij} . Gillet-Chaulet et al. (2006) used a Jeffery's-type equation for A_{ij} valid when the c-axes move by basal slip only. Their model works for arbitrary flow conditions. Gödert (2003) developed a similar model incorporating spherical diffusion into the evolution equation for A_{ij} .

In general, linear anisotropic viscosity must be a fourth order, $3 \times 3 \times 3 \times 3$ tensor \mathbb{F}_{ijkl} . This is because it relates stress and strain rate, two second-order tensors. \mathbb{F}_{ijkl} is a function of the ODF, and also the strain rate if it is a nonlinear constitutive relation. With no simplifications, this is too computationally and analytically difficult for most applications. However, numerous constitutive relations have been developed to account for anisotropy of ice in a more tractable way. The most popular and simple method is to use a scalar enhancement factor as a multiplier of fluidity in Glen's flow law, to adjust for anisotropy or other factors (Lile, 1978). This method is mainly useful under flank flow using the shallow ice approximation. Since only horizontally-directed shear stresses are significant, other stresses and their corresponding viscosity components can be ignored. The enhancement factor is usually chosen empirically. However, the enhancement-factor method is not valid if the ODF does not have a vertical axis of symmetry. In the absence of a vertical axis of symmetry, strain in other components may occur. This makes the assumption of a scalar enhancement factor invalid in these situations (Philip and Meyssonier, 1999).

A number of anisotropic constitutive relations attempt to predict the flow response of a polycrystal from the properties and orientations of individual grains. This brings the problem of homogenization: it is necessary to relate the bulk stress and strain of the entire polycrystal to that experienced by individual grains in a consistent way. There are two possible end members. Homogeneous strain, or the Taylor-Bishop-Hill model (Taylor, 1938), assumes that strain, but not stress, is identical in all grains. This has the advantage of maintaining spatial compatibility among grains. It is a good approximation for materials with several easily-activated slip systems. The homogeneous-strain assumption is an upper bound on the viscous dissipation of energy in the polycrystal: For a given applied bulk strain, the hardest-oriented grains receive the same strain as the easiest-oriented grains. Hard-oriented grains produce more dissipation for the same strain compared to soft-oriented grains. At the other end, the homogeneous stress, or Sachs model (Sachs, 1928), assumes that stress, but not strain, is identical among grains. This is the lower bound on dissipation: For a given strain, easy-oriented grains receive the same stress as hard-oriented grains. Easy-oriented grains thus take a larger proportion of the bulk strain. This reduces dissipation, since the easy-oriented grains produce less dissipation for the same strain. The key disadvantage of the Sachs bound is that spatial compatibility among grains is not maintained. Apart from these, the Visco-Plastic Self-Consistent (VPSC) homogenization scheme (Lebensohn and Tomé, 1993) attempts to more accurately treat homogenization by assuming that each individual grain is an ellipsoidal inclusion in a continuum that has the average properties of the polycrystal (rather than explicitly treating nearest-neighbor interactions). This scheme allows for consistent stress and strain homogenization intermediate between the homogeneous stress and homogeneous strain assumptions. However, the VPSC scheme does not have analytical solutions in general, requiring iterative numerical schemes.

In this paper, we use the homogeneous stress assumption for ice deformation, due to its simplicity. While strain compatibility is violated, the homogeneous stress assumption produces more accurate predictions of rheological properties than homogeneous strain in the case of ice (Thorsteinsson, 2000). This is due to basal slip being by far the most active slip system, with other slip systems accounting for far less strain. Materials with several active slip systems can be more accurately modeled with the homogeneous strain bound. The homogeneous stress assumption is a lower bound on the strength of anisotropy: For a given bulk stress, easy-oriented grains experience more strain. Therefore, we can intuitively expect it to underestimate the strength of the coupling between fabric and flow.

2 Fabric Model

The most important process governing the development of crystal fabrics is deformation-induced grain rotation. If grain deformation is due solely to basal glide, the rate of change of the c-axis orientation is the sum of bulk rotation and viscoplastic spin. From Meyssonnier and Philip (1996), the evolution of c-axis orientation in response to strain can be described by a modified Jeffery's equation (Jeffery, 1922):

$$\dot{c}_i = V_{ij}c_j - D_{ij}c_j + c_ic_jc_kD_{jk}, \quad (2)$$

where c_i is the unit vector in the direction of the c-axis. The tensors V_{ij} and D_{ij} are the vorticity tensor, and local strain-rate tensor of the grain, respectively. The first term gives the rotation rate due to the bulk rotation of the polycrystal, while the second term gives the rotation rate due to viscoplastic spin. Thus, for example, the c-axis of a grain experiencing uniaxial compression will rotate towards the compressive direction. The last term of Jeffery's equation (2) ensures that the motion of grain orientation is tangent to the unit sphere at \mathbf{c} , which is necessary due to the convention that the c-axis vector is of unit length. This can be seen by noting that the $V_{ij}c_j$ term does not affect the magnitude of c_i , leaving only the $D_{ij}c_j$ term. Assume that at time $t = 0$, the c-axis is given by \mathbf{c}_0 . After a short length of time δt , the magnitude of the new c-axis $\mathbf{c}_{\delta t}$ is (without the final term in Eq. 2),

$$||\mathbf{c}_{\delta t}|| = ||\mathbf{c}_0 - \delta t \mathbf{D} \mathbf{c}_0|| \quad (3)$$

$$\approx ||\mathbf{c}_0|| - \mathbf{c}_0^T \mathbf{D} \mathbf{c}_0 \delta t \quad (4)$$

$$= 1 - \mathbf{c}_0^T \mathbf{D} \mathbf{c}_0 \delta t, \quad (5)$$

to first order in δt . Thus, for the c-axis to maintain unit length, we must add the quantity $\mathbf{c}^T \mathbf{D} \mathbf{c} \delta t$ projected onto \mathbf{c} . This then gives the last term of (2).

The above equation gives the evolution of a single grain in response to the applied velocity gradient. It is not practical to integrate this equation for each grain in a polycrystal. Instead, Gillet-Chaulet et al. (2005) derived the following equation for the second-order orientation tensor $A_{ij} = \langle c_i c_j \rangle$ by integrating the material derivative of the structure tensor $c_i c_j$ over the

ODF:

$$\frac{dA_{ij}}{dt} = \langle \dot{c}_i c_j \rangle + \langle c_i \dot{c}_j \rangle. \quad (6)$$

Expressing the material derivative in spatial coordinates yields,

$$\begin{aligned} \frac{\partial A_{ij}}{\partial t} + u_k \frac{\partial A_{ij}}{\partial x_k} = & V_{ik} A_{kj} - A_{ik} V_{kj} - D_{ik} A_{kj} - A_{ik} D_{kj} \\ & + 2\mathbb{A}_{ijkl} D_{kl}, \end{aligned} \quad (7)$$

where D_{ij} is the strain-rate tensor, V_{ij} is the vorticity tensor, and A_{ijkl} is the fourth-order orientation tensor $\langle c_i c_j c_k c_l \rangle$. Unfortunately, the presence of \mathbb{A}_{ijkl} introduces the closure problem. The fourth-order orientation tensor cannot in general be determined from A_{ij} . An ODE for A_{ijkl} can be derived; however it in turn depends on the sixth-order orientation tensor, and so on. Therefore, some kind of an approximation of \mathbb{A}_{ijkl} in terms of A_{ij} must be taken. Here, we use the popular and simple quadratic closure (Advani and Tucker, 1990), where $\mathbb{A}_{ijkl} = A_{ij} A_{kl}$. This closure is accurate whenever the largest eigenvalue $\lambda_3 > 0.8$. It is exact for perfect single-maximum fabrics, where $\lambda_3 = 1$. Deeper layers of ice sheets typically have strong single-maximum fabrics, so this is a good approximation for our purposes.

10 3 Flow Model

We now outline the constitutive relation and physical equations of our flow model. We use the constitutive relation for an orthotropic material with linear transversely isotropic components from Gillet-Chaulet et al. (2005). Let η be the nondimensionalized viscosity of shear in the basal plane. Also, let β be the ratio of viscosity for shear along the basal plane (corresponding to basal slip) to viscosity in shear along orthogonal planes. Let γ be the ratio of viscosity in response to normal stress along the c-axis to the normal stress in the basal plane. We set these parameters to the same values as given by Gillet-Chaulet et al. (2005). We assume $\gamma \approx 1$, because ease of deformation by compression is approximately the same in the c-axis direction as along the basal plane. We set $\beta = 10^{-2}$, and $\eta = 1$. From Gillet-Chaulet et al. (2005), the inverse form of the constitutive relation is given by,

$$\begin{aligned} D_{ij} = \frac{\beta}{2\eta} \Big[& S_{ij} + \xi_1 \mathbb{A}_{ijkl} S_{kl} + \xi_2 (S_{ik} A_{kj} \\ & + A_{ik} S_{kj}) + \xi_3 A_{kl} S_{kl} \delta_{ij} \Big], \end{aligned} \quad (8)$$

20 where,

$$\xi_1 = 2 \left(\frac{\gamma + 2}{4\gamma - 1} - \frac{1}{\beta} \right), \quad \xi_2 = \left(\frac{1}{\beta} - 1 \right), \quad (9)$$

$$\xi_3 = -\frac{1}{3}(\lambda_1 + 2\lambda_2). \quad (10)$$

Stress, as a function of strain rate ($S_{ij} = \mathbb{F}_{ijkl} D_{kl}$), is then found by inverting this relation. The fluidity \mathbb{F}_{ijkl}^{-1} of the constitutive relation given by Eq. (8) is a fourth-order tensor found from the coefficient of S_{ij} , from adding up the terms of Eq. (8). The viscosity in Eq. (8) is also a fourth-order tensor \mathbb{F}_{ijkl} , given by the inverse of \mathbb{F}_{ijkl}^{-1} .

It is often useful to write anisotropic constitutive relations in terms of Voigt notation (Von Mises, 1928), in which symmetric fourth-order tensors are represented as matrices, and symmetric second-order tensors are represented as vectors. The viscosity

\mathbb{F}_{ijkl} can be represented as a 6×6 symmetric matrix \mathbf{F} . Likewise, the symmetric deviatoric stress tensor may be represented as a six-vector \mathbf{s} , where $s_i = S_{ii}$ for $i = 1, 2, 3$, $s_4 = S_{23}$, $s_5 = S_{13}$, and $s_6 = S_{12}$. The case for D_{ij} is identical. Then, the constitutive relation is $s_i = F_{ij}d_j$, where d_i is the Voigt form of D_{ij} .

Along with the constitutive relation, Stokes flow is governed by stress balance and incompressibility,

$$5 \quad \frac{\partial S_{ij}}{\partial x_j} - \frac{\partial p}{\partial x_i} = 0, \quad (11)$$

$$\frac{\partial u_i}{\partial x_i} = 0. \quad (12)$$

The deviatoric stress S_{ij} in Eq. (11) is given by the inverse of Eq. (8).

4 Perturbation approximation

Now we derive an analytical coupled first-order perturbation model from Eqs. (7), (8), (11), (12). We seek to see how a small
10 perturbation to background fabric can grow or decay under this system.

First, assume a background velocity gradient of $\bar{\mathbf{G}}$, homogeneous in all three-dimensional space. We can assume that the velocity vanishes at the origin. The unperturbed velocity at spatial location \mathbf{x} is then given by $\bar{\mathbf{u}} = \bar{\mathbf{G}}\mathbf{x}$. With this background velocity gradient, the unperturbed $\bar{\mathbf{A}}$ may be found from Eq. (7), given initial conditions. Likewise, we can also find the spatially-homogeneous unperturbed deviatoric stress $\bar{\mathbf{S}}$.

15 The unperturbed quantities above are all homogeneous throughout space. Suppose there is now a perturbation of fabric with a single Fourier wavevector $\boldsymbol{\kappa}$. In three-dimensional space, a wavevector rather than a wavenumber is needed to define the orientation of a plane wave. This gives sinusoidal perturbations, where the normal to the plane of the perturbation is the wavevector. See Figure 1 for a cartoon. We perturb the second-order orientation tensor with the replacement $\mathbf{A} \rightarrow \bar{\mathbf{A}} + \epsilon \hat{\mathbf{A}} \cos(\boldsymbol{\kappa} \cdot \mathbf{x})$. The parameter ϵ is small enough that we may neglect ϵ^2 and higher powers. The tensor $\hat{\mathbf{A}}$ is the Fourier coefficient
20 of the perturbation.

Now we seek to derive an approximate evolution equation for the fabric-perturbation Fourier coefficient $\hat{\mathbf{A}}$ (under the assumption that $\epsilon^2 \approx 0$), to see how it grows or shrinks. To first order, there are no spatial Fourier components to any of the other perturbed quantities other than that given by the wavevector $\boldsymbol{\kappa}$. This is because any interaction of perturbations with different wavevectors would be $\mathcal{O}(\epsilon^2)$ or higher, which is negligibly small. Therefore, we can make the following additional
25 replacements,

$$\mathbf{u} \rightarrow \bar{\mathbf{u}} + \epsilon \hat{\mathbf{u}} \sin(\boldsymbol{\kappa} \cdot \mathbf{x}) \quad (13)$$

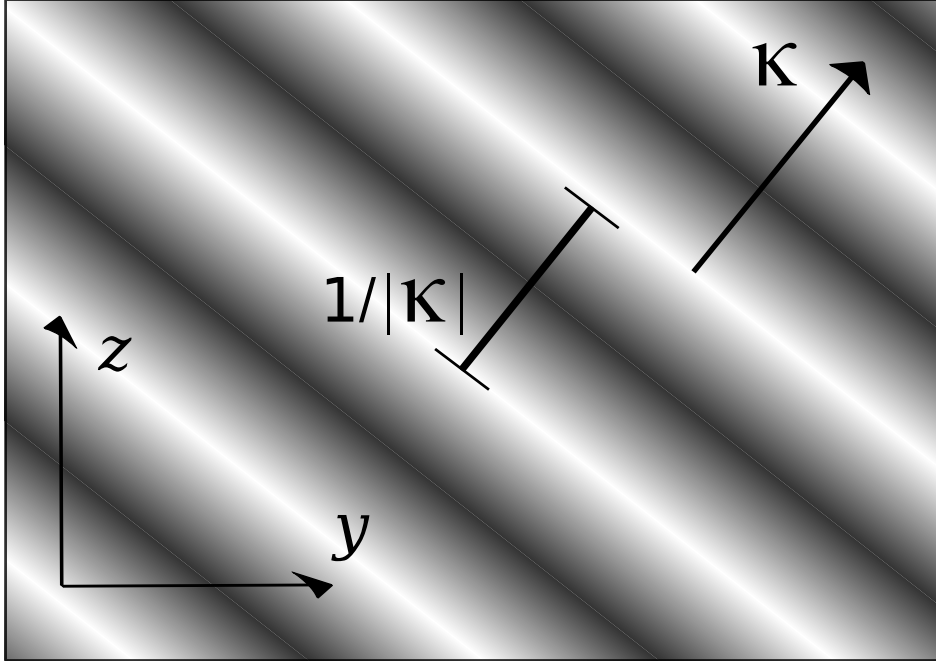
$$\mathbf{S} \rightarrow \bar{\mathbf{S}} + \epsilon \hat{\mathbf{S}} \cos(\boldsymbol{\kappa} \cdot \mathbf{x}) \quad (14)$$

$$\mathbf{D} \rightarrow \bar{\mathbf{D}} + \epsilon \hat{\mathbf{D}} \cos(\boldsymbol{\kappa} \cdot \mathbf{x}) \quad (15)$$

$$p \rightarrow \bar{p} + \epsilon \hat{p} \cos(\boldsymbol{\kappa} \cdot \mathbf{x}) \quad (16)$$

$$30 \quad \mathbf{F} \rightarrow \bar{\mathbf{R}} + \epsilon \hat{\mathbf{F}} \cos(\boldsymbol{\kappa} \cdot \mathbf{x}) \quad (17)$$

Figure 1. Cartoon of the form of a sinusoidal perturbation in space with spatial wavevector κ . The shading represents the sign and magnitude of $\cos(\kappa \cdot \mathbf{x})$, for a perturbation of the form $\hat{c} \cos(\kappa \cdot \mathbf{x})$, where \hat{c} is the Fourier coefficient of the perturbation. The sinusoidal perturbation extends throughout three-dimensional space. The plane of the perturbation is given by the plane that is normal to the wavevector. In this diagram, the positive x -axis extends outwards from the page, and the wavevector lies in the $y - z$ plane.



Now we can define a first-order perturbation to Eq. (7). Discarding higher-order terms, this yields:

$$\left(\frac{\partial}{\partial t} + \bar{\mathbf{u}} \cdot \nabla \right) \left(\hat{A} \cos(\kappa \cdot \mathbf{x}) \right) = \frac{d\hat{A}}{dt} \cos(\kappa \cdot \mathbf{x}). \quad (18)$$

The perturbations themselves are deformed by flow over time, therefore κ is not constant in time. Accordingly, we must find κ consistent with the above equation. To first order, κ is affected only by the unperturbed background flow, which deforms and rotates the planes of perturbations. Given this, we note that by the chain rule,

$$\frac{\partial}{\partial t} \cos(\kappa \cdot \mathbf{x}) = -\frac{d\kappa}{dt} \cdot \mathbf{x} \sin(\kappa \cdot \mathbf{x}) \quad (19)$$

We also have,

$$\bar{\mathbf{u}} \cdot \nabla \cos(\kappa \cdot \mathbf{x}) = -\bar{\mathbf{u}} \cdot \kappa \sin(\kappa \cdot \mathbf{x}) \quad (20)$$

$$= -(\bar{\mathbf{G}}\mathbf{x}) \cdot \kappa \sin(\kappa \cdot \mathbf{x}) \quad (21)$$

The last identity holds because $\bar{\mathbf{u}} = \bar{\mathbf{G}}\mathbf{x}$, where again $\bar{\mathbf{G}}$ is the unperturbed velocity gradient. We can rewrite Eq. (20) as,

$$\bar{\mathbf{u}} \cdot \nabla \cos(\kappa \cdot \mathbf{x}) = -(\bar{\mathbf{G}}^T \cdot \kappa) \cdot \mathbf{x} \sin(\kappa \cdot \mathbf{x}) \quad (22)$$

This identity is more obvious in index notation, since $(\bar{G}_{ij}x_j)\kappa_i = (\bar{G}_{ji}\kappa_i)x_j$. Now, we can rewrite Eq. (18) (noting that $\nabla \hat{\mathbf{A}} = 0$) as,

$$\begin{aligned} \frac{d}{dt} \left(\hat{\mathbf{A}} \cos(\boldsymbol{\kappa} \cdot \mathbf{x}) \right) &= \left(\frac{\partial}{\partial t} + \bar{\mathbf{u}} \cdot \nabla \right) \left(\hat{\mathbf{A}} \cos(\boldsymbol{\kappa} \cdot \mathbf{x}) \right) \\ &= \frac{\partial \hat{\mathbf{A}}}{\partial t} \cos(\boldsymbol{\kappa} \cdot \mathbf{x}) + \hat{\mathbf{A}} \frac{\partial}{\partial t} \cos(\boldsymbol{\kappa} \cdot \mathbf{x}) \\ &\quad + \hat{\mathbf{A}} (\bar{\mathbf{u}} \cdot \nabla \cos(\boldsymbol{\kappa} \cdot \mathbf{x})) \\ &= \frac{\partial \hat{\mathbf{A}}}{\partial t} \cos(\boldsymbol{\kappa} \cdot \mathbf{x}) - \bar{\mathbf{G}} \mathbf{x} \cdot \boldsymbol{\kappa} \sin(\boldsymbol{\kappa} \cdot \mathbf{x}) \\ &\quad - \frac{d\boldsymbol{\kappa}}{dt} \cdot \mathbf{x} \sin(\boldsymbol{\kappa} \cdot \mathbf{x}) \end{aligned} \quad (23)$$

The last identity follows from Eqs. (19) and (22). For this equation to be satisfied, the last two terms involving sines must cancel out. Therefore, we require that

$$\frac{\partial}{\partial t} \boldsymbol{\kappa} = -\bar{\mathbf{G}}^T \boldsymbol{\kappa}. \quad (24)$$

This is an ODE system for $\boldsymbol{\kappa}$. The solution for an initial wavevector $\boldsymbol{\kappa}(0)$ and a constant velocity gradient is,

$$\boldsymbol{\kappa}(t) = \exp(-t\bar{\mathbf{G}}^T) \boldsymbol{\kappa}(0). \quad (25)$$

Since fabric evolution is dependent on flow, we now see how the fabric perturbation affects the flow equations (8), (11), and (12). We will solve these flow equations to get perturbations of velocity and pressure, and from that substitute the perturbed velocity gradient back into Eq. (7) (while discarding higher-order terms).

Now, we substitute these perturbed quantities into the flow equations (11) and (12), and neglect terms of $\mathcal{O}(\epsilon^2)$ and higher. The perturbed fluidity in Voigt notation, $\hat{\mathbf{F}}^{-1}$, is found by substituting $\bar{\mathbf{D}} + \epsilon \hat{\mathbf{D}} \cos(\boldsymbol{\kappa} \cdot \mathbf{x})$ into Eq. (8), then subtracting out the unperturbed fluidity, and removing terms of $\mathcal{O}(\epsilon^2)$ and higher. The spatially-variable $\cos(\boldsymbol{\kappa} \cdot \mathbf{x})$ appears in every term, and can be canceled out. This removes any dependence on the spatial location \mathbf{x} . Then, using a well-known matrix inverse identity, the Fourier component of the perturbation of viscosity is given by $\hat{\mathbf{F}} = -\bar{\mathbf{F}} \hat{\mathbf{F}}^{-1} \bar{\mathbf{F}}$, to first order. We can then use this to find the Fourier coefficient of the deviatoric stress perturbation, $\hat{\mathbf{S}}$, if we know the perturbations to stress and strain. First, we find the Fourier coefficient $\hat{\mathbf{G}}$ of the perturbed velocity gradient. The perturbation to velocity is given by $\epsilon \hat{\mathbf{u}} \sin(\boldsymbol{\kappa} \cdot \mathbf{x})$. We then have,

$$\nabla (\epsilon \hat{\mathbf{u}} \sin(\boldsymbol{\kappa} \cdot \mathbf{x})) = \epsilon \hat{\mathbf{u}} \otimes \boldsymbol{\kappa} \cos(\boldsymbol{\kappa} \cdot \mathbf{x}) \quad (26)$$

Using this, we can write the Fourier coefficient of the velocity-gradient perturbation as,

$$\hat{\mathbf{G}} = \nabla \mathbf{u} \frac{1}{\epsilon \cos(\boldsymbol{\kappa} \cdot \mathbf{x})} = \hat{\mathbf{u}} \otimes \boldsymbol{\kappa} \quad (27)$$

The Fourier coefficients of the perturbations to strain rate, vorticity, and stress respectively follow as,

$$\hat{\mathbf{D}} = \frac{1}{2} (\hat{\mathbf{G}} + \hat{\mathbf{G}}^T), \quad (28)$$

$$\hat{\mathbf{V}} = \frac{1}{2} (\hat{\mathbf{G}} - \hat{\mathbf{G}}^T), \quad (29)$$

$$\hat{\mathbf{s}} = \hat{\mathbf{F}} \bar{\mathbf{d}} + \bar{\mathbf{F}} \hat{\mathbf{d}}, \quad (30)$$

5 where \mathbf{s} and \mathbf{d} are respectively the deviatoric stress and strain tensors represented in Voigt notation. Force balance and incompressibility perturbations are found by substituting the perturbed deviatoric stress ($\bar{\mathbf{S}} + \epsilon \cos(\boldsymbol{\kappa} \cdot \mathbf{x}) \hat{\mathbf{S}}$) and pressure ($\bar{p} + \epsilon \cos(\boldsymbol{\kappa} \cdot \mathbf{x}) \hat{p}$) into the flow equations (11) and (12). After canceling out the spatially variable $\sin(\boldsymbol{\kappa} \cdot \mathbf{x})$ from each equation, this yields the algebraic system,

$$\hat{\mathbf{S}} \boldsymbol{\kappa} + \boldsymbol{\kappa} \hat{p} = 0, \quad (31)$$

$$10 \quad \boldsymbol{\kappa} \cdot \hat{\mathbf{u}} = 0. \quad (32)$$

Knowing the Fourier coefficient $\hat{\mathbf{A}}$ of the perturbation to the second-order orientation tensor, we can now use Eq. (31) and Eq. (32) to analytically solve for the perturbed $\hat{\mathbf{u}}$ and \hat{p} , and in turn $\hat{\mathbf{D}}$ and $\hat{\mathbf{V}}$. This yields solutions for $\hat{\mathbf{D}}$ and $\hat{\mathbf{V}}$ as functions of the known quantities $\boldsymbol{\kappa}$, $\hat{\mathbf{A}}$, $\bar{\mathbf{A}}$, $\bar{\mathbf{V}}$, and $\bar{\mathbf{D}}$. We did this using Wolfram Mathematica™. The code is available in the supplementary material. This yields,

$$\begin{aligned} \frac{d\hat{\mathbf{A}}}{dt} &= \mathcal{Q}(\hat{\mathbf{A}}, \bar{\mathbf{A}}, \bar{\mathbf{D}}, \bar{\mathbf{V}}, \boldsymbol{\kappa}) \\ &= \hat{\mathbf{V}} \bar{\mathbf{A}} + \bar{\mathbf{V}} \hat{\mathbf{A}} - \hat{\mathbf{A}} \bar{\mathbf{V}} - \bar{\mathbf{A}} \hat{\mathbf{V}} - \hat{\mathbf{D}} \bar{\mathbf{A}} - \bar{\mathbf{D}} \hat{\mathbf{A}} - \hat{\mathbf{A}} \bar{\mathbf{D}} \\ &\quad - \bar{\mathbf{A}} \hat{\mathbf{D}} + 2 \left(\hat{\mathbf{A}} \bar{\mathbf{A}} \bar{\mathbf{D}} + \bar{\mathbf{A}} \hat{\mathbf{A}} \bar{\mathbf{D}} + \bar{\mathbf{A}} \bar{\mathbf{A}} \hat{\mathbf{D}} \right) \end{aligned} \quad (33)$$

This is a system of ordinary differential equations. Again, $\hat{\mathbf{V}}$ and $\hat{\mathbf{D}}$ depend on $\boldsymbol{\kappa}$, $\hat{\mathbf{A}}$, $\bar{\mathbf{A}}$, $\bar{\mathbf{V}}$, and $\bar{\mathbf{D}}$. However, we do not write $\hat{\mathbf{V}}$ and $\hat{\mathbf{D}}$ in terms of these quantities, because the derived expressions are long. They may be generated using the code in the supplementary material. Next, we linearize Eq. (33) about $\hat{\mathbf{A}} = 0$, with $\hat{\mathbf{A}}$ being represented in Voigt notation by the six-vector $\hat{\mathbf{a}}$. This then gets us the Jacobian of the system, given by,

$$20 \quad \mathbf{J} = \left. \frac{\partial \mathbf{q}}{\partial \hat{\mathbf{a}}} \right|_{\hat{\mathbf{a}}=0} (0, \bar{\mathbf{A}}, \bar{\mathbf{D}}, \bar{\mathbf{V}}, \boldsymbol{\kappa}) \quad (34)$$

where \mathbf{q} is \mathcal{Q} (Equation 33) in Voigt notation. Again, we derived this Jacobian using Wolfram Mathematica™. This defines the linearized ODE for $\hat{\mathbf{a}}$ about $\hat{\mathbf{a}} = 0$:

$$\frac{d\hat{\mathbf{a}}}{dt} = \mathbf{J} \hat{\mathbf{a}}. \quad (35)$$

The solution to Eq. (35) for an initial perturbation $\hat{\mathbf{a}}_0$ at time $t = 0$ is,

$$25 \quad \hat{\mathbf{a}}(t) = \exp(\mathbf{J}t) \hat{\mathbf{a}}_0, \quad (36)$$

where the \exp is the matrix exponential. The Jacobian matrix \mathbf{J} can be diagonalized as $\mathbf{Q}\mathbf{Z}\mathbf{Q}^{-1}$, where \mathbf{Q} are the right eigenvectors of \mathbf{J} , and \mathbf{Z} is a diagonal matrix of eigenvalues ζ_i of \mathbf{J} . Then the above equation reduces to,

$$\hat{\mathbf{a}}(t) = \mathbf{Q} \exp(\mathbf{Z}t) \mathbf{Q}^{-1} \hat{\mathbf{a}}_0. \quad (37)$$

Here, the matrix exponential reduces to the ordinary exponential function applied elementwise to the diagonal of \mathbf{Z} . From this, it can be seen that the eigenvalues ζ_i of \mathbf{J} give the stability of the system as a function of the unperturbed second-order orientation tensor ($\bar{\mathbf{A}}$), velocity gradient ($\bar{\mathbf{G}}$), and wavevector ($\boldsymbol{\kappa}$) of the perturbation. If there is an eigenvalue ζ_i with a positive real part, then the system is unstable about the equilibrium $\hat{\mathbf{A}} = 0$. This can be seen from Eq. (37): If $\text{Re}[\zeta_i] > 0$, then, $\exp(\mathbf{Z})_{ii} = \exp(\zeta_i t)$ (no sum) is an exponential with a positive real part which grows as t increases. A small nudge in the direction of the corresponding eigenvector will grow. Note that the eigenvectors of this system are characteristic perturbations of $\bar{\mathbf{a}}$ in Voigt notation, or $\bar{\mathbf{A}}$ in standard notation. The corresponding eigenvalues give the growth rates of the corresponding characteristic perturbation of $\bar{\mathbf{A}}$. Thus, they may be thought of as “eigenmatrices.” In the next section, we examine the stability of this system for different flow regimes and perturbation wavevectors.

5 Results

We now present results for layered perturbations at different angles to homogeneous, unperturbed flow. We examine the cases where the unperturbed flow is either pure shear or simple shear along horizontal layers. To do this, we forced the perturbation model with wavevectors rotated about the x - or y -axes at a range of different angles from vertical. This corresponds to having layered perturbations whose planes are rotated from horizontal by the same angles. We assume an nondimensionalized effective strain rate of unity in both cases. This also defines a characteristic time scale. We also assume that $\|\boldsymbol{\kappa}\| = 1$, corresponding to layers that are non-dimensionalized to be unit thickness. We plot the real part of the largest eigenvalue of the linearized system for each flow scenario. This gives the perturbation of \mathbf{A} with the fastest growth rate. Note that a perturbation eigenvalue may be interpreted as a growth rate of the paired perturbation “eigenvector” of \mathbf{A} . We examine only the real parts of the eigenvalues (which are complex in general) because the imaginary part corresponds to spinning about the fixed point of the perturbation (where $\hat{\mathbf{a}} = 0$), and is not as relevant to stability. The eigenvalues and eigenvectors come in conjugate pairs. This ensures that real initial conditions yield real solutions.

In this section, we will make use of first-order approximations to perturbations of eigenvectors and eigenvalues (Trefethen and Bau III, 1997) to interpret fabric perturbations. Suppose we have a perturbation $\epsilon \cos(\boldsymbol{\kappa} \cdot \mathbf{x}) A_{ij}$ to an element of the second-order orientation tensor \mathbf{A} of a vertical single-maximum fabric. We choose to work in a reference frame such that the direction of maximum concentration is vertical, and \mathbf{A} is diagonal. In this reference frame, the diagonal elements \hat{A}_{ii} (no sum) are the perturbations to the corresponding eigenvalues of \mathbf{A} , to first order. The off-diagonal elements give the Euler angles of the rotation of the fabric principal directions due to the perturbation, to first order. The element $\epsilon A_{13} \cos(\boldsymbol{\kappa} \cdot \mathbf{x})$ is the Euler angle of rotation about the y -axis. The cases of the other off-diagonal elements are similar.

5.1 Layered perturbations in simple shear

First, we take the background flow to be simple shear along horizontal planes, with the unperturbed component of the velocity-gradient tensor $\bar{G}_{13} = 2$, and other components set to zero. In Figure 2, we plot the real part of the eigenvalue of the Jacobian \mathbf{J} with the maximum growth rate, ζ_{max} (in other words, the growth rate of the perturbation with the highest growth rate) for wavevectors rotated about the x -axis from vertical by several different angles. Note that the largest unperturbed fabric eigenvalue, λ_3 , is plotted on the horizontal axis. Similarly, Figure 3 shows the growth rates for perturbations whose wavevectors are rotated from vertical about the y -axis. We do not plot results for perturbations in horizontal layers. The coupled ODE (Equation 34) is not differentiable at the origin, $\hat{\mathbf{A}} = 0$ in this case, rendering the linearization invalid.

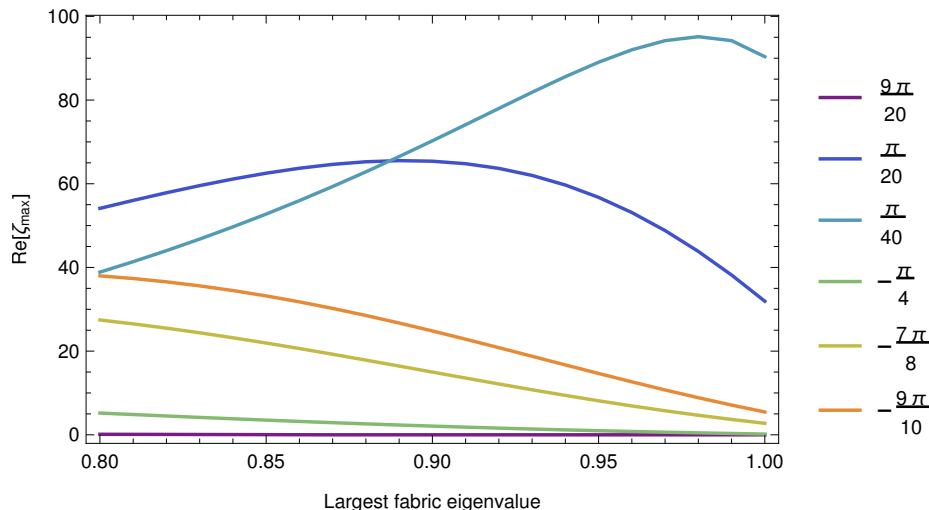
In Table 2, we show the characteristic perturbation $\hat{\mathbf{A}}$ associated with the Jacobian eigenvalue ζ_{max} for several different largest fabric eigenvalues λ_3 , and for wavevectors (normal to the planes of perturbation) rotated from horizontal about the x - or y -axis.

Perturbations along planes with shallow dips either the x - or y -directions (with small angles of rotation from horizontal) have high growth rates. Perturbations along planes with steep dips in either direction have much smaller growth rates. Maximum growth rates are generally higher for dips in the x -direction, along the flow (corresponding to a rotation about the y -axis).

The characteristic perturbations with maximum growth rates for perturbations whose planes have shallow dips (see Table 2) have straightforward interpretations for strong fabrics. For perfect single-maximum fabrics ($\lambda_3 = 1$) whose planes of perturbation tilt away from horizontal in the x -direction (along the direction of shear), the Fourier coefficient \hat{A}_{ij} of the characteristic perturbation with the highest growth rate is $\hat{A}_{ij} = \delta_{i1}\delta_{j3} + \delta_{i3}\delta_{j1}$. In other words, the only nonzero elements of $\hat{\mathbf{A}}$ are $A_{13} = A_{31}$. This corresponds to an infinitesimal rotation of the vertical single-maximum fabric about the y -axis, either towards the plane of perturbation, or away, depending on the phase (given by $\cos(\boldsymbol{\kappa} \cdot \mathbf{x})$). For regions where the fabric is rotated toward the plane of perturbation, the rotation brings the basal planes of the constituent crystals in greater alignment with the plane of perturbation, and the c -axes in greater alignment with the wavevector of the perturbation. This enhances shear along the plane of perturbation, since shear along basal planes is by far the easiest mode of deformation in ice. Note that the perturbations examined in this paper can only produce shear along the plane of perturbation, due to the incompressibility constraint (Equation 12). In turn, greater shear along the plane of perturbation causes faster rotation of c -axis towards the wavevector normal to the plane of perturbation, resulting in further growth of the perturbation. In regions where the fabric is rotated away from the plane of perturbation, the shear component along that direction is retarded, producing a velocity perturbation in the opposite direction.

The case for perturbations tilt away from horizontal in the y -direction, corresponding to a rotation about the x -axis, is somewhat similar. The difference is that the characteristic perturbation \hat{A}_{ij} associated with the highest growth rate instead corresponds to a rotation of the single-maximum fabric about both the x -axis and y -axis, with both $A_{13} \neq 0$ and $A_{23} \neq 0$. This results in a velocity perturbation oriented diagonally from the direction of flow, parallel to the plane of perturbation, and orthogonal to the wavevector.

Figure 2. Growth rates of perturbations in simple shear dipping in the y direction. The largest real part of the eigenvalues ζ the Jacobian matrix (34) under simple shear in the x direction, as a function of the largest fabric eigenvalue λ_3 . Each curve represents the growth rate of a perturbation whose wavevector has been rotated by a different angle θ about the x -axis.



The characteristic perturbations \hat{A}_{ij} with the fastest growth rate for weaker single-maximum fabrics ($\lambda_3 < 1$) also include perturbations to the diagonal elements of \mathbf{A} . To first order, these correspond to perturbations of the fabric eigenvalues. The perturbations to diagonal elements alternately strengthen or weaken the single-maximum fabric, depending on the sign of $\sin(\kappa \cdot x)$. However, the perturbations of off-diagonal elements, corresponding to rotations of the fabric about the x -axis ($\hat{A}_{23} \neq 0$) or y -axis ($\hat{A}_{13} \neq 0$) are typically of larger magnitude.

Table 2. The real part of the eigenvalue (or, growth rate) of the eigenvalue with the highest real part, and Fourier coefficients \hat{A}_{ij} of the associated characteristic perturbation of the second-order orientation tensor \mathbf{A} , for perturbations whose planes of perturbation are rotated from horizontal by a rotation of ϕ about the y -axis, or a rotation of θ about the x -axis, and for different choices of largest eigenvalue λ_3 . We also show the Fourier coefficients of the associated velocity perturbations, \hat{u}_i . The unperturbed background flow is simple shear.

λ_3	θ	ϕ	$\text{Re}(\zeta_{max})$	\hat{A}_{11}	\hat{A}_{22}	\hat{A}_{33}	\hat{A}_{32}	\hat{A}_{13}	\hat{A}_{12}	\hat{u}_1	\hat{u}_2	\hat{u}_3
1	0	$\pi/100$	233	0	0	0	0	1	0	-0.83	0	0.026
0.95	0	$\pi/10$	14	-0.04	-0.023	0.063	0	-1	0	-0.19	0	0.061
0.95	0	$-4\pi/5$	1	0.18	0.13	-0.32	0	0.92	0	-0.023	0	0.017
0.99	$-7\pi/8$	0	3.7	0.0069	0.009	-0.016	0.52	-0.85	0.0018	-0.49	-0.47	-0.19
1.	$\pi/50$	0	105	0	0	0	-0.7	0.74	0	-4.9	-1.9	-0.12
0.8	$\pi/5$	0	9.8	0.086	0.16	-0.25	-0.36	0.88	0.081	0.82	0.24	0.17

Figure 3. Growth rates of perturbations in simple shear dipping in the x direction. The largest real part of the eigenvalues of the Jacobian matrix (34) under simple shear in the x direction, as a function of the largest fabric eigenvalue λ_3 . Each curve is a perturbation whose wavevector has been rotated by a different angle ϕ about the y -axis.

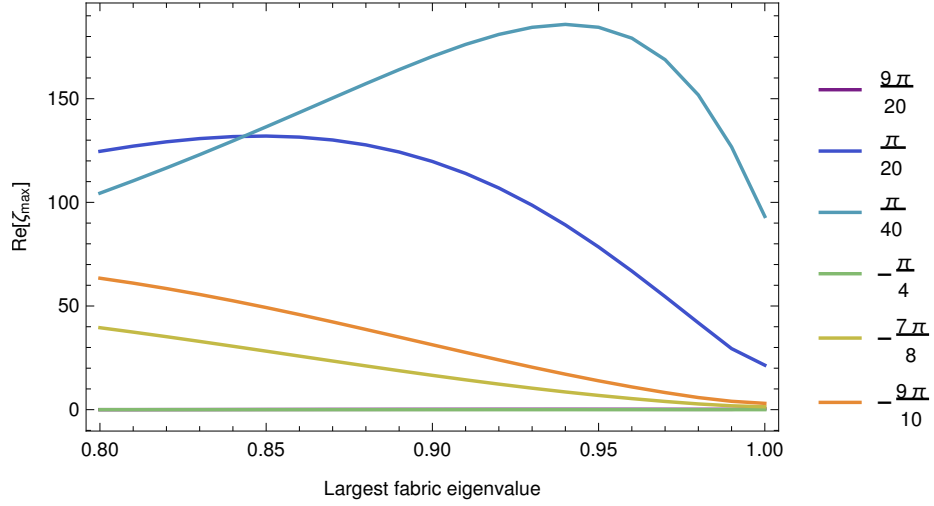


Figure 4. The largest real part of the eigenvalues of the Jacobian matrix (34) under pure shear, as a function of the largest fabric eigenvalue λ_3 . Each curve is a perturbation whose wavevector has been rotated by a different angle ϕ about the y -axis.

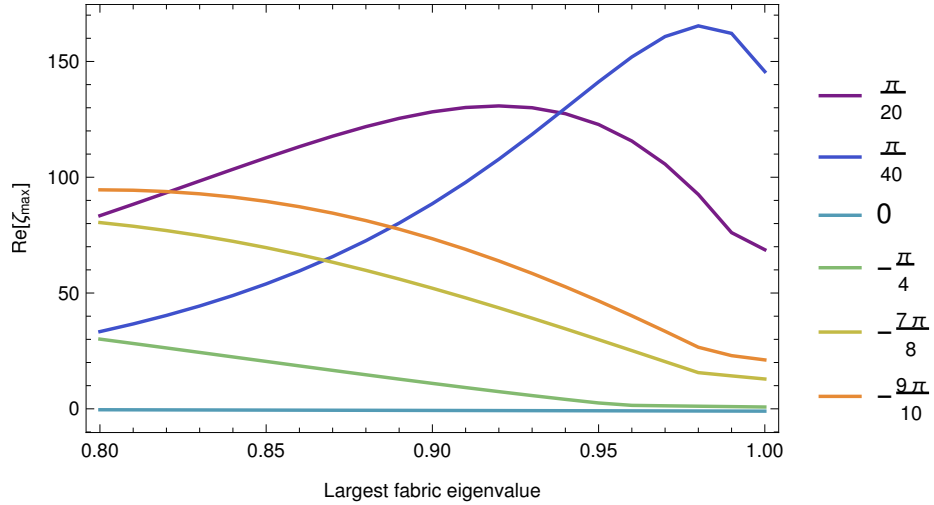


Figure 5. The largest real part of the eigenvalues of the Jacobian matrix (34) under pure shear, as a function of the largest fabric eigenvalue λ_3 . Each curve is a perturbation whose wavevector has been rotated by a different angle θ about the x -axis.

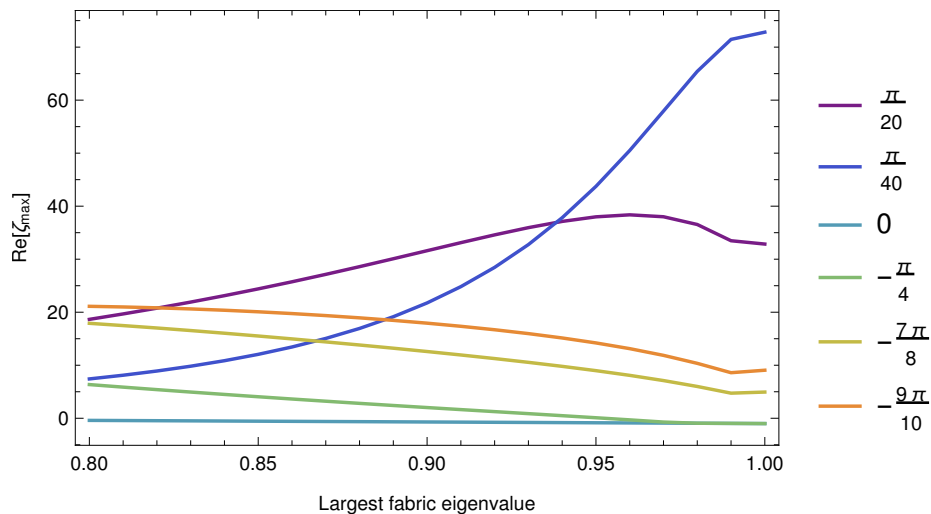


Table 3. The real part of the eigenvalue (or, growth rate) of the eigenvalue with the highest real part, and Fourier coefficients \hat{A}_{ij} of the real characteristic perturbation of the second-order orientation tensor \mathbf{A} associated with that eigenvalue, for perturbations whose planes of perturbation are rotated from horizontal by a rotation of ϕ about the y -axis, or a rotation of θ about the x -axis, and for different choices of largest eigenvalue λ_3 . The unperturbed background flow is pure shear. As with simple shear, perturbations along layers with shallow, but nonzero, dips have higher growth rates.

λ_3	θ	ϕ	$\text{Re}(\zeta_{max})$	\hat{A}_{11}	\hat{A}_{22}	\hat{A}_{33}	\hat{A}_{23}	\hat{A}_{13}	\hat{A}_{12}	\hat{u}_1	\hat{u}_2	\hat{u}_3
1	0	0	-1	0	0	0	1	0	0	0	0	0
1	0	$\pi/40$	146	0	0	0	0	1	0	0.53	0	-0.042
0.8	0	$\pi/40$	33	0.03	0.014	-0.046	0	1	0	0.6	0	0.046
0.8	0	$\pi/4$	30	-0.36	-0.16	0.51	0	-0.77	0	-0.72	0	0.72
1	0	$49\pi/100$	-1.25	0	0	0	1	0	0	-0.005	-0.14	0.16
1.	$\pi/40$	0	73	0	0	0	1	0	0	0	-0.3	-0.019
0.8	$\pi/40$	0	7.2	0.011	0.031	-0.042	1	0	0	0	-0.014	-0.011

5.2 Layered perturbations under pure shear

We now examine perturbations to single-maximum fabrics under pure shear, such as near an ice divide. The real part of the Jacobian eigenvalue (or, growth rate) with the highest real part, ζ_{max} , for perturbations whose plane of perturbation has been rotated from horizontal about the y -axis, is shown in Figure 4. In Figure 5, we show the growth rates for perturbations whose

planes of perturbation have been rotated about the x -axis. Lastly, we show maximum growth rates ζ_{max} along with their corresponding characteristic perturbations several different wavevector orientations and fabric strengths in Table 3.

The results are broadly similar to the case of simple shear. Perturbations to strong single-maximum fabrics along planes with shallow, but nonzero dips in both the x direction and y direction are unstable in pure shear. Perturbations along steeply-inclined planes (with wavevectors closer to horizontal) are stable, with $\zeta_{max} < 0$.

For a perfect vertical single-maximum fabric, where all c -axes are vertical, $A_{ij} = \delta_{i3}\delta_{j3}$. In this case, for all perturbations possessing high growth rates, whose wavevector has been rotated from vertical about the y -axis, the Fourier component \hat{A}_{ij} of the perturbation to A_{ij} associated with the highest perturbation growth rate is given by $\hat{A}_{ij} = \delta_{i3}\delta_{j1} + \delta_{j3}\delta_{i1}$. In other words, the only nonzero components of the Fourier coefficient of the perturbation to A_{ij} with the highest growth rate are $\hat{A}_{13} = \hat{A}_{31} = 1$.

This form of perturbation has a similar interpretation to the case of simple shear. For a perfectly concentrated vertical single-maximum fabric in pure shear, there is no resolved shear stress on the basal planes of any grain, thus every grain is in the hardest orientation possible. The perturbation $\hat{A}_{ij} = \delta_{i3}\delta_{j3} + \delta_{j3}\delta_{i3}$, represents an infinitesimal rotation of the fabric about the y -axis. This changes the predominant alignment of basal planes with respect to the plane of perturbation (either an increase or decrease depending on $\sin(\boldsymbol{\kappa} \cdot \boldsymbol{x})$). This results in shear strain perturbation along the plane of perturbation, producing a velocity perturbation parallel to the plane, orthogonal to the y direction (i.e., $\hat{u}_2 = 0$).

The case for perturbations whose plane of perturbation tilted in the y direction (or a rotation from horizontal about the x axis) is similar, except that growth rates are generally smaller. For perfect vertical single-maximum fabrics, the only nonzero elements of $\hat{\mathbf{A}}$ are $\hat{A}_{23} = \hat{A}_{32}$, corresponding to an infinitesimal rotation of the vertical single-maximum fabric about the x -axis. Depending on the sign of $\sin(\boldsymbol{\kappa} \cdot \boldsymbol{x})$, this alternately increases or decreases the resolved shear stress on the plane of perturbation, resulting a velocity perturbation along the plane of perturbation, orthogonal to x -direction, such that $\hat{u}_1 = 0$.

6 Discussion

In the flow scenarios considered, dynamic instability seems to be the rule rather than the exception. An important constraint to the flow perturbations is that the perturbed velocity must be orthogonal to the wavevector, and parallel to the plane of the perturbations. This can be seen from the incompressibility constraint (Equation 32) in the perturbation model, $\hat{\mathbf{u}} \cdot \boldsymbol{\kappa} = 0$. Since the velocity perturbation is $\epsilon \hat{\mathbf{u}} \sin(\boldsymbol{\kappa} \cdot \boldsymbol{x})$, this means that the velocity perturbation must be orthogonal to the wavevector. Thus, if the wavevector is vertical, then there cannot be a vertical component to the velocity perturbation. The perturbed velocity gradient must consist solely of shear orthogonal to the wavevector. To overturn stratigraphic layers in ice sheets, there must be a vertical-velocity component. However, a layer needs to be tilted only a small amount to produce a vertical-velocity perturbation, and fabric perturbations on layers with shallow but nonzero dips tend to have higher growth rates. Depending on the sign of $\sin(\boldsymbol{\kappa} \cdot \boldsymbol{x})$, in the Lagrangian frame of the unperturbed flow, this perturbation moves some ice upwards, and other ice downwards.

For strong fabrics, fabric perturbations of single-maximum with the highest growth rates in simple shear and pure shear are infinitesimal rotations of the single-maximum fabric which alternately increase or decrease the misalignment of the fabric

eigenvector associated with the largest eigenvalue (corresponding to the largest c-axis concentration) and the wavevector, depending on the phase (given by $\sin(\kappa \cdot x)$). This brings the basal planes of the c-axis fabric in greater (or lesser) alignment with the plane of perturbation (orthogonal to the wavevector). This alternately eases or inhibits shear along the plane of perturbation, again depending on the phase. Velocity perturbations in response to the fabric perturbation only occur in shear parallel to the plane of perturbation, thus this enhances the velocity perturbation associated with the fabric perturbation. Where the sign of $\sin(\kappa \cdot x)$ is such that the plane of perturbation progressively rotates c-axes towards the direction of the wavevector of the perturbation, shear is further increased along the plane of perturbation, yielding a positive feedback. In parts of the phase where the fabric is rotated away from the plane of perturbation, shear is inhibited, and the velocity perturbation occurs in the opposite direction, yielding a positive feedback as well.

Growth rates of perturbations in this model can be high in comparison to the characteristic time of the unperturbed background deformation. However, it is important to keep in mind some of the limitations of this model. It is applicable only to perturbations with thicknesses sufficiently smaller than the ice sheet. For thick layers, the effects of the ice-sheet boundaries become more important, violating the assumptions of this model. The scale of perturbations must also be large enough that the ice can be treated as a continuum. In addition, it is a first-order model, valid for small perturbations. As perturbations become larger, higher-order effects (which this model does not capture) become important. However, the stability of perturbations in this model can show in which situations perturbations can develop in the first place.

Even with a high growth rate, a sufficiently small initial perturbation could take quite some time to grow large. For this reason, we do not expect large perturbations to develop in upper layers of ice sheets. However, perturbations may have enough time to develop in the lower layers of ice sheets. This may be especially true for flank flow, where simple shear dominates in basal layers. The high shear stress near the bed would accelerate the growth of the perturbations. It is possible that the effects of coupled flow on perturbations, studied in this paper, may reinforce the development of perturbations from other sources. Disturbed layering is ubiquitous in deeper layers of ice sheets, and any flow disturbances will also have a corresponding effect on fabric. Disturbances due to basal topography, spatially-variable recrystallization, or basal freeze-on may provide additional means of seeding fabric perturbations.

7 Conclusions

Due to the strong viscous anisotropy of ice as a function of c-axis orientation fabric, it is important to understand flow of anisotropic ice as a coupled system. To this end, we developed a first-order coupled perturbation model of fabric evolution and flow of anisotropic ice.

We examined the stability of the system under various perturbations and flow scenarios. Under this model, coupled ice flow and fabric evolution is unstable across a wide range of flow and fabric conditions: certain forms of fabric perturbations are reinforced, and grow through positive feedback between flow and fabric. For strong fabrics, the perturbations with the highest growth rates are infinitesimal rotations of the unperturbed fabric which are effective at promoting or inhibiting shear (depending on the phase) along the plane of perturbation.

Fabric perturbations in this model are capable of causing vertical offsets in both both simple shear and pure shear. This is a potential mechanism for stratigraphic disturbances in ice. The instabilities would not occur in fabric that is uncoupled to flow. These types of perturbations may help explain the small-scale stratigraphic disturbances seen far above the bed in ice sheets. In addition, it provides a means of growth for fabric perturbations from other sources. The results from this analytical
5 model demonstrate the insufficiency of two-dimensional, plane flow models in understanding anisotropic flow. Small, out-of-plane fabric perturbations in unperturbed plane flow can grow, violating the assumptions of two-dimensional plane flow. This reinforces the fact that flow of anisotropic ice and fabric development is a fundamentally three-dimensional problem.

Further numerical simulations of macroscopic coupled flow and fabric would shed more light on the development of perturbations. The two-dimensional numerical model of coupled fabric and plane flow in Gillet-Chaulet et al. (2006) seems to
10 show large spatially-variable contrasts in fabric developing in response to basal topography. Additional numerical simulations, especially three-dimensional ones, in a range of different flow scenarios, and with a range of initial fabric perturbations, would be useful.

References

- Advani, S. and Tucker, C.: Closure approximations for three-dimensional structure tensors, *Journal of Rheology*, 34, 367–386, 1990.
- Alley, R.: Flow-law hypotheses for ice-sheet modeling, *J. Glaciol*, 38, 245–256, 1992.
- Alley, R., Gow, A., Meese, D., Fitzpatrick, J., Waddington, E., and Bolzan, J.: Grain-scale processes, folding, and stratigraphic disturbance
5 in the GISP2 ice core, *Journal of Geophysical Research*, 102, 26 819–26, 1997.
- Azuma, N.: A flow law for anisotropic ice and its application to ice sheets, *Earth and Planetary Science Letters*, 128, 601–614, 1994.
- Azuma, N. and Goto-Azuma, K.: An anisotropic flow law for ice-sheet ice and its implications, *Annals of Glaciology*, 23, 202–208, 1996.
- Fudge, T., Taylor, K., Waddington, E., Fitzpatrick, J., and Conway, H.: Electrical stratigraphy of the WAIS Divide ice core: Identification of
centimeter-scale irregular layering, *Journal of Geophysical Research: Earth Surface*, 121, 1218–1229, 2016.
- 10 Gillet-Chaulet, F., Gagliardini, O., Meyssonier, J., Montagnat, M., and Castelnau, O.: A user-friendly anisotropic flow law for ice-sheet
modelling, *Journal of glaciology*, 51, 3–14, 2005.
- Gillet-Chaulet, F., Gagliardini, O., Meyssonier, J., Zwinger, T., and Ruokolainen, J.: Flow-induced anisotropy in polar ice and related
ice-sheet flow modelling, *Journal of Non-Newtonian Fluid Mechanics*, 134, 33–43, 2006.
- Gödert, G.: A mesoscopic approach for modelling texture evolution of polar ice including recrystallization phenomena, *Annals of Glaciology*,
15 37, 23–28, 2003.
- Jansen, D., Llorens, M., Westhoff, J., Steinbach, F., Kipfstuhl, S., Bons, P., Grier, A., and Weikusat, I.: Small-scale disturbances in the
stratigraphy of the NEEM ice core: observations and numerical model simulations, *The Cryosphere*, 10, 359–370, 2016.
- Jeffery, G.: The motion of ellipsoidal particles immersed in a viscous fluid, *Proceedings of the Royal Society of London. Series A, Containing
papers of a mathematical and physical character*, pp. 161–179, 1922.
- 20 Lebensohn, R. and Tomé, C.: A self-consistent anisotropic approach for the simulation of plastic deformation and texture development of
polycrystals: application to zirconium alloys, *Acta Metallurgica et Materialia*, 41, 2611–2624, 1993.
- Lile, R.: The effect of anisotropy on the creep of polycrystalline ice, *Journal of Glaciology*, 21, 475–483, 1978.
- Meyssonier, J. and Philip, A.: A model for the tangent viscous behaviour of anisotropic polar ice, *Annals of Glaciology*, 23, 253–261, 1996.
- Montgomery-Smith, S.: Perturbations of the coupled Jeffery-Stokes equations, *Journal of Fluid Mechanics*, 681, 622–638, 2011.
- 25 Philip, A. and Meyssonier, J.: Anisotropic isothermal ice-cap flow with the shallow ice approximation, in: *Advances in Cold-Region
Thermal Engineering and Sciences*, pp. 237–248, Springer, 1999.
- Sachs, G.: Zur Ableitung einer Fließbedingung, *Z. Vereins Dtsch. Ing.*, 12, 734–736, 1928.
- Svendsem, B. and Hutter, K.: A continuum approach for modelling induced anisotropy in glaciers and ice sheets, *Annals of Glaciology*, 23,
262–269, 1996.
- 30 Taylor, G.: Analysis of plastic strain in a cubic crystal, *Stephen Timoshenko 60th Anniversary Volume*, pp. 218–224, 1938.
- Thorsteinsson, T.: Anisotropy of ice Ih: Development of fabric and effects of anisotropy on deformation, Ph.D. thesis, University of Wash-
ington, 2000.
- Thorsteinsson, T. and Waddington, E.: Folding in strongly anisotropic layers near ice-sheet centers, *Annals of Glaciology*, 35, 480–486,
2002.
- 35 Trefethen, L. N. and Bau III, D.: *Numerical linear algebra*, vol. 50, Siam, 1997.
- Von Mises, R.: Mechanics of plastic deformation of crystals, *Applied Mathematics and Mechanics*, 592, 8, 1928.